A new paramagnetically shifted imaging probe for MRI

Journal:	*Magnetic Resonance in Medicine*
Manuscript ID	Draft
Wiley - Manuscript type:	Full Paper
Date Submitted by the Author:	n/a
Complete List of Authors:	Senanayake, P; Durham Univeristy, Chemistry Rogers, Nicola; Durham Univeristy, Chemistry Finney, Katie-Louise; Durham Univeristy, Chemistry Harvey, peter; Durham Univeristy, Chemistry Funk, Alexander; University of Texas Southwestern Medical Center at Dallas Wilson, J; Newcastle University, Northern Institute for Cancer Research O'Hogain, Dara; Newcastle University, Institute of Cellular Medicine Maxwell, Ross; Newcastle University, Northern Institute for Cancer Research Parker, David; Durham University, Department of Chemistry Blamire, Andrew; Newcastle University, Institute of Cellular Medicine
Research Type:	Contrast agents < Contrast < Biophysics < Technical Research
Research Focus:	No specific tissue or organ focus

A new paramagnetically shifted imaging probe for MRI

P. Kanthi Senanayake[3], Nicola J. Rogers[3], Katie-Louise N. A. Finney[3], Peter Harvey[3], Alexander M. Funk[3], J. Ian Wilson[2], Dara O'Hogain[1], Ross Maxwell[2], David Parker[3], Andrew M. Blamire*[1]

Affiliations:

1: Institute of Cellular Medicine & Newcastle MR Centre, Newcastle University

2: Northern Institute for Cancer Research, Newcastle University

3: Dept. of Chemistry, Durham University, South Road, Durham.

Corresponding author:

Andrew M. Blamire,

Newcastle Magnetic Resonance Centre,

Campus for Ageing and Vitality,

Newcastle University,

Newcastle upon Tyne, NE4 5PL

United Kingdom:

Tel: +44 191 208 1150

Fax: +44 191 208 1151

E-mail: andrew.blamire@newcastle.ac.uk

Running Title: PARASHIFT imaging for molecular MRI

Word Count: 4837

Abstract

Purpose: To develop and characterize a new paramagnetic contrast agent for molecular imaging by MRI.

Methods: A contrast agent was developed for direct MRI detection through the paramagnetically shifted proton magnetic resonances of 2 chemically equivalent *tert*-butyl reporter groups within a dysprosium(III) complex. The complex was characterized in phantoms and imaged in physiologically intact mice at 7T using 3D gradient echo and spectroscopic imaging (MRSI) sequences to measure spatial distribution and signal frequency.

Results: The reporter protons reside ~6.5Å from the paramagnetic center, resulting in fast T_1 relaxation (T_1 = 8ms) and a large paramagnetic frequency shift exceeding 60 ppm. Fast relaxation allowed short scan repetition times with high excitation flip angle, resulting in high sensitivity. The large dipolar shift allowed direct frequency selective excitation and acquisition of the dysprosium(III) complex, independent of the tissue water signal. The biokinetics of the complex were followed *in vivo* with a temporal resolution of 62s following a single, low dose intravenous injection. The lower concentration limit for detection was ~23μM. Through MRSI the temperature dependence of the paramagnetic shift (0.28 ppm.K^{-1}) was exploited to examine tissue temperature variation.

Conclusion: These data demonstrate a new MRI agent with potential for physiological monitoring by MRI.

Keywords

Contrast agent, molecular imaging, paramagnetic shift, temperature mapping.

Introduction

Contrast agents are routinely used to improve the diagnostic specificity of MRI. The most commonly used agents are based on chelated gadolinium in which the local dipolar field of the Gd ion causes an increase in the longitudinal relaxation rate (R_1) of water molecules within the local vicinity (and can also increase tissue R_2* via local susceptibility effects). The presence of the contrast agent is inferred from the resulting intensity change of the water signal using T_1 or T_2* weighted MRI respectively. These contrast systems are entirely passive, accumulating and being removed from tissues by diffusive processes only, with regionally differing contrast enhancement arising from local rates of delivery, accumulation and clearance (1). A new frontier for MRI contrast agent design is to create functionalized probes which target specific aspects of cellular or physiological properties of the disease under investigation. Agents which bind to a range of targets, such as collagen in fibrotic scar tissue (2-4) or the endothelial wall (5,6), have been developed. All of these agents also rely on indirect detection via changes in water relaxation rates (R_1, R_2 or R_2*) through conventional gadolinium chelates (1) or iron oxide systems (7), rather than detecting the contrast molecule directly.

The presence of the lanthanide metal ion within a contrast agent acts on nuclei in the local structure of the chelating molecule and can induce large paramagnetic shifts, yielding distinct resonances that can be detected, offering the possibility of directly detecting the agents themselves. Several studies have examined this effect as a mechanism to create molecular imaging agents, typically using thulium complexes ($TmDOTA^-$ or $TmDOTMA^-$). In these cases proton groups within the DOTA or DOTMA structures are paramagnetically shifted by tens to hundreds of ppm from the water signal and so can lie far beyond the biological proton resonant frequency range. Frequency selective acquisition can then be used to detect these signals independent of the main water peak (8-11). The magnitude of the paramagnetic shift is sensitive to physiological conditions including temperature (10-12) and pH (12,13), conveying functionality to these molecules. Previous studies have demonstrated the feasibility of *in vitro* (10,11) and *in vivo* (8-10,14-19) molecular imaging of these agents and highlighted the challenge in obtaining sufficient sensitivity, with the majority of studies using high dose i.v. injection (5 to 10 times clinical contrast dose) and renal ligation to prevent the normal clearance of contrast from blood to sustain an artificially enhanced tissue and vascular concentration.

Certain studies have examined the use of different lanthanide metals (9,11), but have not sought to optimize the chelator to both maximize reporter group structure and optimize

relaxivity properties, which are essential factors in defining overall measurement sensitivity. We have previously developed a small molecular weight ^{19}F-labelled lanthanide metal chelate, in which the structure was manipulated such that the dipolar field of the metal enhanced the longitudinal relaxation rate of the ^{19}F nuclei. Increasing R_1 allowed rapid pulsing in the MR experiment, lowering the detection threshold to ca. 20μM of complex (20,21). Here, we apply the same principles of lanthanide enhanced relaxation and design a new chelate with two chemically equivalent proton reporter groups to provide extremely favorable operating conditions for high sensitivity molecular MRI, whilst retaining the extremely large paramagnetic shift of the proton reporter group. The detected MR signal from the reporter groups is outside the biological proton resonant frequency range, allowing 3-dimensional imaging of the molecular probe against zero background. As an exemplar of using this type of agent as a physiological probe, regional tissue temperature variation was determined *in vivo* using MR spectroscopic imaging. To distinguish this direct detection approach from other indirect MR detection methods of similar lanthanide probes (for example PARACEST, (22)) we earlier suggested the term PARASHIFT agents when describing such lanthanide MR contrast agents (23).

Methods

The study was conducted in 2 main parts. Firstly the PARASHIFT agents were synthesized and NMR relaxation properties measured to determine the structural characteristics of the complex. Secondly, the relaxation data was used to define optimal scanning conditions and *in vivo* imaging, biodistribution analysis and tissue temperature mapping studies were undertaken in mice.

Synthesis and characterization of PARASHIFT agents

A cyclen-based dysprosium(III) complex ($[Dy.L^1]^-$) and its gadolinium analogue ($[Gd.L^1]^-$) were designed focusing on a high number of reporter protons and their relaxivity as the main design criteria. The complex incorporates two *tert*-butyl reporter groups giving 18 equivalent protons whose resonance signal was to be detected directly. The synthesis and characterization of $[Dy.L^1]^-$ and $[Gd.L^1]^-$ was undertaken using established methodology (Scheme 1/Supporting Material), as described in recent work (23,24). The longitudinal relaxation rate of the reporter group depends on the nature of the local field experienced by those protons and varies with lanthanide ion, whereas the presence of a non-spherical

electronic distribution produces the dipolar paramagnetic shift, with a magnitude dependent upon the distance and angle of the reporting nuclei to the paramagnetic center. Our criteria were that R_1 must be high to allow fast pulsing and the paramagnetic shift must be sufficient to allow the shifted reporter resonance to be excited and detected separate to the tissue signals from water and fat. The shift must therefore be greater than the imaging readout bandwidth in order that there can be no contamination of the PARASHIFT image by residual water or fat signal. Based on our previous work Dy was found to have more favorable relaxation properties than Tm, Tb or Ho (23,24) and so $[Dy.L^1]^-$ was chosen for PARASHIFT imaging, whereas $[Gd.L^1]^-$ was synthesized for standard MR contrast imaging.

High-resolution NMR field-dependent R_1 measurements were made, examining the *tert*-butyl resonance. The nuclear relaxation times of the *tert*-butyl group of $[Dy.L^1]^-$ were measured at 6 field strengths (4.7, 9.4, 11.7, 14.1 and 16.5 Tesla) at 295 K using the inversion-recovery technique (see Supporting Material). The nuclear relaxation data was fitted by using a modified Matlab algorithm originally written by Dr. Ilya Kuprov (Southampton University). The algorithm uses the Solomon-Morgan-Bloembergen equation (Eq. 1) to fit measured relaxation data using Levenberg-Marquardt minimization of the non-linear squares error function, from which the electron-nuclear distance r was estimated.

$$R_1 = \frac{2}{15}\left(\frac{\mu_0}{4\pi}\right)^2 \frac{\gamma_N^2\, g_{Ln}^2\, \mu_B^2\, J(J+1)}{r^6}\left[\frac{3T_{1e}}{1+\omega_N^2 T_{1e}^2} + \frac{7T_{1e}}{1+\omega_e^2 T_{1e}^2}\right] + \frac{2}{5}\left(\frac{\mu_0}{4\pi}\right)^2 \frac{\omega_N^2\, \mu_{eff}^4}{(3k_B T)^2\, r^6}\left[\frac{3\tau_r}{1+\omega_N^2 \tau_r^2}\right] \quad \text{[Eq 1]}$$

where μ_0 is vacuum permeability, γ_N is the nuclear gyromagnetic ratio, g_{Ln} is the Landé factor of the Ln ion, μ_B is the Bohr magneton, τ_r is the rotational correlation time, ω_N is the nuclear Larmor frequency, ω_e is the electron Larmor frequency and μ_{eff} the effective magnetic moment. The results were analyzed iteratively assuming that longitudinal and transverse electronic relaxation times (T_{1e} and T_{2e}) were of similar magnitude.

MRI studies – General Details

In vivo imaging studies were performed using a 7T preclinical MRI system (20cm bore, Varian Direct Drive scanner, Agilent, Palo Alta, CA) equipped with a 39mm i.d. quadrature birdcage RF coil (Rapid Biomedical GmbH, Germany) for excitation and detection of the water and PARASHIFT agent signals. Mice were mounted in a dedicated

bed including a pneumatic pillow system to measure and gate acquisition to animal respiration and a fiber-optic thermometry system for temperature monitoring and control via a warm air system (SA Instruments Inc., Stony Brook, NY). Mice were anaesthetized using isoflurane and an i.v. line was inserted into a tail vein to allow injection of contrast agent from outside of the magnet. No other surgical preparation was used. To confirm positioning and visualize regional anatomy conventional spin-echo MRI scans were collected on the water resonance (TR/TE=2200 (gated) / 10.93 ms, 45 × 1 mm thick slices, field of view FOV 35 × 35 mm, matrix 256 × 256).

All animal experiments were reviewed and approved by the Newcastle University (UK) animal welfare committee, and were performed complying with the UK Government Home Office under the animals (scientific procedure) act 1986.

Gd uptake and biodistribution study

Biodistribution of the complexes was first studied using the Gd analogue in four HCT116 tumor-bearing CD1 Nu/Nu Nude mice (Charles River, UK), although the analysis only focused on normal tissues. Tissue uptake and clearance of the complex was examined by dynamic contrast enhanced (DCE) MRI using $[Gd.L^1]^-$ providing T_1w contrast on conventional MRI. Slices were chosen through liver and kidneys. Gradient echo scans were acquired every 6 seconds for 60 minutes commencing 5 images before administration of the contrast agent (dose of 0.1 mmol/kg $[Gd.L^1]^-$, in a volume of 200µl given over 6 seconds). MRI parameters were: TR/TE= 23.45/4.40 ms; flip angle 30^o, 2 mm slice thickness, FOV 40 × 40 mm, matrix 256 × 256. DCE images were analyzed using ImageJ software (http://imagej.nih.gov/ij/) to extract image intensity changes over time. Regions of interest (ROI) were drawn on liver, kidney, muscle and bladder and mean ROI intensity measurements calculated for each time point. Data were normalized to the mean background level pre-contrast injection.

Following MRI, mice were sacrificed by cervical dislocation and tissues excised immediately and freeze clamped in liquid nitrogen. To obtain tissue concentrations over time a further series of animals (n = 3 per time point) were injected with $[Gd.L^1]^-$ and sacrificed at 10, 20, 40 and 80 min post injection. In all cases three separate tissue samples were taken from the kidney and liver and stored at -80^{o}C prior to analysis. Plasma samples were taken at each time point and frozen. Samples were analyzed for Gd content using ICP-mass spectrometry (see Supporting Material).

PARASHIFT dynamic imaging studies

PARASHIFT studies using the $[Dy.L^1]^-$ were performed in CD1 wild type mice (Charles River, UK) without any implanted tumor (n=6). Unlike previous *in vivo* studies using i.v. injection of paramagnetically shifted agents (8,9,14-18,25), our animals were physiologically intact, without renal ligation. Animals were positioned in the birdcage coil and a 20 mm long, 5 mm diameter NMR tube phantom containing ~100μL of 6mM solution of PARASHIFT agent positioned under the body of the animal to allow for system calibration (scanner frequency) and to act as an external reference for quantitation. This phantom was fastened to a line that allowed it to be withdrawn from the imaging FOV following calibration to avoid contamination of the *in vivo* signal from the phantom. Measurements were made in three groups of animals using three different methods to illustrate different aspects of the PARASHIFT molecular signal.

Measurement 1 – Optimized imaging of regional contrast distribution

For simple detection of the agent *in vivo* an optimized 3D gradient-echo (3DGE) sequence was employed. Our previous work has shown that once an imaging spectral width (SW) is defined (which, with the choice of imaging matrix size determines the minimum TE), the scan should be collected at the shortest available TR under Ernst angle conditions (21). The minimum allowed SW for these experiments is defined by the fat-PARASHIFT frequency difference. At the 7T operating frequency of 300MHz this frequency difference (1.5 to -61ppm) corresponds to ~20kHz. By restricting the imaging bandwidth to 20 kHz and applying a sharp digital filter to the data, images of the water or PARASHIFT peak were collected simply by shifting the excitation and acquisition center frequency of the scan. Signal excitation used a non-spatially selective 1 ms duration Gaussian excitation pulse with a FWHM bandwidth of 2100Hz, falling to a fractional excitation of $<10^{-3}$ at 20kHz, which completely eliminated any observable contaminating signal from one resonance while imaging the other. Scan parameters were: TE/TR=1.45/2.87 ms (ungated), 20 kHz spectral width, axial FOV 64×64 mm, matrix 32×32, 16 encodes in the 3rd direction covering a slab thickness of 240 mm yielding 15 mm thick slices. Scans used 42 signal averages for a total duration of 61.7s per dataset. Pulse flip angle was calibrated to the Ernst angle of 46^{o}, (which is possible for these experiments because the PARASHIFT R_1 is known and fixed by the *intra-molecular* interaction with the Ln ion, independent of tissue concentration). Dual detection of non-overlapping water and PARASHIFT images were also collected by using

signal excitation at the PARASHIFT frequency with double receiver bandwidth of 40 kHz centered between the water and PARASHIFT frequencies and double the number of readout matrix points.

The RF excitation power was calibrated on the water signal and then the system was retuned to the PARASHIFT frequency using the phantom signal. Imaging FOV was positioned based on standard proton MRI and the 3DGE sequence collected. This scan provided intensity reference data for the PARASHIFT phantom from which *in vivo* studies were quantified. The phantom was then withdrawn from the FOV and a repeat 3DGE sequence collected to ensure the image matrix was free of any signal from tissue water. Dynamic time series of 3DGE scans were then collected commencing with the injection of 200µl of PARASHIFT agent (0.04 mmol/kg $[Dy.L^1]^-$), followed by saline flush and continuing for 30 minutes. Following PARASHIFT imaging the system was retuned to the water frequency and a high quality conventional MRI scan was collected as an anatomical reference image using a standard multislice SE sequence (respiratory gated TR/TE= 2200/10.9 ms, 50 × 1 mm thick slices, FOV 35 × 35 mm, matrix 256 × 256).

PARASHIFT images were analyzed using ImageJ software to extract image intensity changes over time. ROI were drawn on tissues of interest (liver, kidney and bladder) and mean ROI intensity values extracted for each time point. The pre-injection dataset containing the PARASHIFT filled phantom was used as the concentration standardization reference level. The mean signal from pixels placed centrally within the phantom (completely filled with solution) was determined and PARASHIFT tissue concentration curves were calculated as the ratio of the ROI mean signal relative to the phantom, scaled by phantom concentration (6mM). A ROI placed outside the animal was used to measure the background noise floor in the scans, to estimate the detection limit of the contrast agent.

Measurement 2 – Spectroscopic imaging

To demonstrate detection of the signal spectroscopically rather than by imaging, 2D and 3D spectroscopic imaging sequences were used. Sequence parameters for 2DSI were TR/TE=4.46/0.70 ms, FOV 64×64mm, matrix16×16, spectral sweep width 20kHz, 64 data points. Scans used 53 signal averages with scan duration of 61s. The resulting data was 3 dimensional (2 spatial, 1 spectroscopic) with the spatial dimension localizing a thick axial (XY) plane condensing all detail along the Z direction of the magnet. Sequence parameters for 3DSI were TR/TE=7.69/0.73 ms, FOV 32×32×64 mm, matrix 16×16×8 resulting in 8mm thick axial slices. Spectral sweep width was 20kHz with 128 data points. Scans used 4 signal

averages with scan duration 63 s. For the 3D sequence, the resulting data was 4 dimensional (3 spatial, 1 spectroscopic). In both cases signal excitation again used the same 1 ms non-selective Gaussian pulse as in the 3DGE imaging studies.

Measurement 3 - Temperature mapping studies

The chemical shift of the PARASHIFT signal is sensitive to sample temperature and therefore can be used for temperature mapping. To determine the temperature coefficient, *in vitro* measurements of the frequency shift against temperature were made for the $[Dy.L^1]^-$ complex in both deuterated water and rat plasma using standard temperature controlled high-resolution NMR over the range 298-318K spanning room to body temperature.

In vitro temperature mapping studies were made using a sample of $[Dy.L^1]^-$ in a 5mm NMR tube which was warmed in a water bath to 40^{o}C and then placed in a polystyrene thermal insulating sleeve and imaged every 60s as it cooled to room temperature. Sample temperature was monitored with the *in vivo* thermometry system. Measurements were made using a 2DSI sequence with TR/TE=27.05/0.7 ms, spectral width 20kHz, 512 sample points, 90^o Gaussian excitation, FOV 32 × 32 mm, matrix 32 × 32 and a single average for an acquisition time of 27s. The 2DSI data were processed via 3 dimensional Fourier transformation, including 75Hz exponential line-broadening in the spectral domain. The frequency of the PARASHIFT line was determined at each temperature by peak peaking. To ensure frequency shifts were due only to temperature and not to differences in local B_o field strength, a separate reference scan was collected at the water frequency. Data were also presented as images displaying signal intensity at a specific spectral frequency.

In vivo temperature mapping studies were performed in CD1 mice using the same experimental protocol as the imaging experiments but with the spectroscopic imaging sequence. The *in vivo* measurements used a 3DSI sequence with TR/TE=7.69/0.70 ms, spectral width 20 kHz, 128 sample points, 90^o Gaussian excitation, FOV 32 × 32 × 64 mm, matrix 16 × 16 × 8 and 4 averages for a total acquisition time of 63 s per dataset. Measurements were made pre-injection and at 1, 2, 3, 4, 5 and 25 minutes post injection. The 3D spectroscopic imaging data were processed via 4 dimensional Fourier transformation, including 75Hz exponential line-broadening in the spectral domain. Maps of local tissue concentration of agent were created by integration of peak area for every pixel in the 3D spatial volume. Regional temperature differences were determined from peak frequency changes.

Results

The structure of the [Ln.L^1] complex is shown in Figure 1a. The proton spectrum of [Dy.L^1]$^-$ (Figure 1b) shows the PARASHIFT signal from the major isomer at -60.1ppm, (295K, a frequency shift of ~20,000Hz relative to water at 7T) and the minor isomer (12%) at -63.8ppm. The reporter group to metal ion distance was estimated to be 6.5 (±0.1)Å, following previous density functional theory (DFT) calculations of similar structures (24). This estimate is supported by the excellent fit between the high-resolution NMR field-dependent R_1 measurements of the *tert*-butyl group and Bloch-Redfield-Wangsness theory (23,24) using a distance of 6.5Å (Fig. 1c). It is important to stress that the spectral peak arises directly from the *tert*-butyl protons and that the R_1 relaxation rate is independent of injected concentration – a fundamental distinction from conventional MR agents where the water relaxation rate varies proportionally with instantaneous contrast agent concentration in the tissue. Relaxivity R_1 was measured at 7T to be 128s^{-1}, with R_2 of 227s^{-1} (R_1/R_2 = 0.56). Phantom images illustrating the acquisition of 3DGE images from the individual water or PARASHIFT resonances and using simultaneous dual PARASHIFT-water acquisition are shown in Fig. 1d.

The results of the biokinetics study of the complex using [Gd.L^1]$^-$ and DCE-MRI (conventional, indirect T_1 contrast) are shown in Figure 2. The DCE-MRI data demonstrated a biphasic kinetic profile in the kidney with an early peak around 2 minutes arising mainly from the intravascular signal of the injected agent (Fig. 2a), followed by a second broader peak as the complex exchanged in and out of body tissues and was finally cleared through the kidneys. In muscle the tissue contrast peaked at around 5 minutes and then decayed away over the ensuing 40 minutes, with the [Gd.L^1]$^-$ complex eventually becoming visible in the bladder and continually increasing over the following 45 minutes (data not shown). Tissue Gd concentration was separately analyzed by inductively coupled plasma mass spectroscopy of excised tissue, and strongly paralleled the MRI data, as expected (Fig. 2b and 2a).

The PARASHIFT molecular MRI measurements (direct detection of the *tert*-butyl group of the [Dy.L^1]$^-$ complex) are illustrated in Figure 3. Passage of the agent through the tissue could be followed by 3D imaging (Fig. 3a) and ROI analysis demonstrated similar biokinetics to the Gd analogue (Fig. 3b). Mean peak SNR was 14.8 (range 8.9 to 22.1) in kidney, 7.2 (range 4.0 to 10.0) in liver and 30.0 (range 12.7 to 45.5) in bladder. Since the signal in the PARASHIFT images arises from the molecule itself and the R_1 relaxation rate is intrinsic to the *intra*-molecular interaction, the signal was simply quantified against the external reference standard solution acquired under the same conditions. Peak concentration

of PARASHIFT agent measured in the kidney and liver ROIs was determined to be 200±90 and 90±20 μmol dm^{-3} respectively. Under these experimental conditions, the detection limit, as determined by the noise floor in the scans, was estimated to be 23 μmol dm^{-3}.

The relationship between PARASHIFT frequency and sample temperature was determined *in vitro* to be linear over the range 298-318K (Supp. Figs. S1-S3 and Fig. 4) with a temperature coefficient of 0.25±0.03 ppm/K in D_2O and 0.28±0.01 ppm/K in mouse plasma. At the 7T field used for imaging this corresponds to 84 Hz/K, so is small enough not to cause spatial distortion in the image formation process (image bandwidth 312.5 Hz per pixel), but is sufficiently large to allow accurate measurement by optimized MRSI. Temperature mapping data from the *in vitro* study is illustrated in Figure 4a. Spectroscopic imaging detection allowed the PARASHIFT peak frequency to be measured *in vivo* and converted to tissue temperature (Fig. 4b) based on the previously measured temperature coefficient. While the animals were maintained at a core body temperature of 37°C the shift mapping studies demonstrated temperature variations between tissues over time which decreased by 348Hz (4.1 K) between initial detection of the intravascular signal and arriving in the bladder.

Discussion

MRI is an inherently insensitive detection method and the ability to obtain direct molecular images by MRI under thermal equilibrium magnetization conditions is limited to compounds with tissue concentrations typically in the low millimolar range. Approaches to enhance the sensitivity to molecular targets have used conjugation of the target molecule to large reporter compounds such as iron oxide particles which yield contrast via indirect (and often diffuse) through-space interactions, or other inter-molecular interactions via chemical exchange, such as in CEST and PARACEST (22) methods. The use of paramagnetically shifted resonances arising from nuclei within the structure of the target molecule (8,9,15,17-19,23) offers an alternative method based on small molecule structures, but optimization of the chelator structure to maximize imaging sensitivity has seen little systematic investigation.

Relaxivity is a key factor in defining detection sensitivity. By manipulating the intra-molecular distances from the lanthanide ion to the reporter group, the R_1 relaxation rate can be increased allowing the MR sequence to be run rapidly and with high flip angle, maximizing signal collection per unit time (21). R_1 for the $[Dy.L_1]^-$ probe was $128s^{-1}$ at 7T rising to $160s^{-1}$ at 9.4T and $185s^{-1}$ at 11.7T which is slightly lower than the relaxivity of the

H-3 protons in [TmDOTMA] (reported to be 188 s^{-1} at 9.4T (9) and 211 s^{-1} at 11.7T,(16)) and substantially lower than for the H-6 protons of TmDOTP (reported as 625 s^{-1} at 11.7T, (16)). While this might suggest TmDOTP has preferred properties, sensitivity is not solely defined by R_1, but also by transverse signal decay (R_2) which reduces overall signal. The very high reported R_2 for TmDOTP at 11.7T (1369s^{-1}, (16)) means transverse signal loss are significant for imaging and linewidths extremely broad for spectroscopic detection. R_1/R_2 for TmDOTMA are reported as 0.883 at 11.7T (16) and 0.774 at 9.4T (9) but excretion is very fast and the structure presents no opportunity for structural modification as the equivalence of the 4 Me groups or 4 H on the ring is lost by anything other than C-4 symmetric tetra-substitution.

Choice of the lanthanide metal is fundamental to the magnitude of the paramagnetic shift, as has been illustrated here for dysprosium (60 ppm shift) and gadolinium (no shift). Selection of other lanthanide ions such as Tb, Tm or Er, provide agents with different properties both in terms of reporter group relaxation rates and also paramagnetic shift. The more commonly studied thulium complexes show paramagnetic shifts from 140ppm (11) to more than 200ppm (9), while previous characterization of similar Ln structures to that used here shows that shifts ranging from around -80 to +70ppm are achievable (24). Our recent work suggests that these shifts are not entirely predicted by current theory (26), but the experimentally demonstrated shifts offer opportunities for more advanced imaging approaches.

Prior work seeking to observe paramagnetically shifted ligand resonances has been limited by the need for large doses, almost always requiring the use of renally ligated animals to eliminate clearance of the agent, or the use of continuous infusion to maintain sufficient signal intensity. For example, the use of the rapidly cleared complexes, $[Tm.DOTP]^{5-}$ or $[Tm.DOTMA]^{-}$ has been examined (8,14) in which the temperature and pH dependence of a shifted resonance was monitored by spectral imaging in rats undergoing continuous infusion to maintain a complex concentration in the blood of the order of 2-3 mmol/kg. In the current work we successfully imaged the dynamics of the complex using a single i.v. injection in an intact animal at a dose of 0.04 mmol/kg of $[Dy.L^1]^{-}$. Previous studies have also achieved high spatial resolution of 1μl voxels (14), but again this has only been possible using high administered doses in combination with small surface coils, leading to restricted FOV. In studying dynamics our focus was on temporal rather than spatial resolution and we therefore selected a lower spatial resolution. However, taking into account differences in B_o field

strength, scan duration, total complex administered and the sensitivity differences between surface coils and our volume coil (27) we calculate that our data show a sensitivity improvement of a factor of 5 over this high resolution study (14) and factors of between and 20 (18) and 60 (9,16,17) against other recent studies using $[TmDOTMA]^-$. These numbers are conservative estimates as they make no allowance for our use of a single i.v. injection. More recently, $[Tm.DOTMA]^-$ has been used in cell-labelling studies *in vivo*, where the complex was internalized inside the cell population prior to injection (19) which highlights an area for further evaluation of our complex.

We have demonstrated the ability to measure our agent *in vivo* at a low tissue concentration of 23μmol dm^{-3}, similar to the detection threshold for a fluorine based compound we have previously reported (21). Further increases in sensitivity require higher signal level per molecule and slower clearance. Increasing the signal is possible in imaging experiments through the use of partial Fourier acquisition or ultrashort TE (UTE) imaging (19) to reduce signal loss from transverse relaxation. In theory a factor of ~1.3 is achievable from the relaxation loss during the current 1.45ms TE and the R_2 of our molecule ($227s^{-1}$). The rate of clearance and excretion of the contrast agent is also relatively high. Altering structure, such as conjugation of multiple copies to a larger molecule (28) can be used to change biodynamics and further enhance detection sensitivity.

We have demonstrated temperature mapping using this agent as a simple physiological probe, although we acknowledge temperature can be measured using conventional water MRI. Future developments will modify the molecule to place a substituent next to the t-butyl group whose shift is sensitive to pH creating a pH probe. Co-injection of PARASHIFT agents with different functional properties (e.g. sensitivity to pH, T, etc.) and with different Ln ions selected to produce opposing shifts into upfield and downfield regions of the spectrum can then allow monitoring of multiple processes *in vivo*, simply by selection of the appropriate bandwidth and resonant frequency. A further possibility is to consider these types of structures as "building blocks" for more complex forms. Alternatively, linking structures based around only one species of Ln metal but with different paramagnetic shifts engineered via different Ln ion, reporter group distances could produce multi-functional probes. An example here would be to create dual-probes with distinguishable signals which are physiologically sensitive and insensitive to provide an internally referenced scan intensity. Dual or multi-probe systems would also have the advantage that biodynamics for each group would be guaranteed to be identical.

An important alternate strategy for molecular MRI employs chemical exchange effects (e.g. chemical exchange saturation transfer, CEST, imaging). This approach is again an indirect detection method which measures a change in the bulk (tissue) water signal as a result of saturation of a frequency shifted proton which is undergoing chemical exchange between the molecular tracer of interest and the bulk water itself. The frequency shift may be due to natural chemical shift effects (29) or due to induced shifts from injected paramagnetic ions (PARACEST approaches (22,30)). In the case of PARACEST agents the indirect nature of the detection continues to be a challenge when determining absolute concentration for many cases of molecule. While a number of agents have been synthesized and evaluated for sensitivity to physiological parameters *in vitro* (reviewed in (31)), relatively few have been successfully demonstrated *in vivo* (32-38), and in some cases have used direct injection into tissue of interest and/or high injected doses to obtain high local tissue concentrations. Recently PARACEST agents have been used in mouse models to measure extracellular pH (36-38) and enzyme activity (35). In the context of the previous CEST based work, it is again important to stress that the PARASHIFT approach we describe here is entirely distinct and in no way relates to chemical exchange effects.

Conclusions

The current study has demonstrated a new chelator structure for high sensitivity PARASHIFT molecular imaging *in vivo*. We have shown that this agent can be detected using clinically relevant doses and can be used to report simultaneously on tissue concentration and physiological parameters, e.g. tissue temperature.

Acknowledgements

This work was supported by grants from Engineering and Physical Sciences Research Council (EPSRC), award number EP/L012189/1 and the European Research Council, award number 266804. The authors acknowledge the assistance of Dr Chris Ottley (Earth Sciences, Durham University) who carried out ICP-MS analyses.

Figure Legends:

Scheme 1

Synthesis scheme for the $[Ln.L^1]^-$ complexes, where Ln was either Gd or Dy.

Figure 1: Structure and properties of the PARASHIFT complex

a) Structure of $[Ln.L^1]^-$

b) Proton spectrum collected on a 7 T preclinical imaging scanner from the *tert*-butyl signal region (centered at -60.1 ppm) for $[Dy.L^1]^-$. The signal was measured from 100 μL of 6 mM solution using a volume imaging coil, with a 1ms long Gaussian 90° excitation pulse, 20 kHz spectral width, TR = 55 ms, 32 averages and a total acquisition time of 1.76 s. The long RF pulse was used to narrow the bandwidth and prevents excitation of water, but leads to a first order phase difference between the major and minor resonances. The major resonance at -60.1 ppm yields 88% of the signal with the minor resonance at -63.8 ppm the remaining 12% signal.

c) Longitudinal relaxation rates for $[Dy.L^1]^-$ as a function of magnetic field, (D_2O 295 K) showing the fit (line) of the Solomon-Morgan-Bloembergen equation to the data (fixed r = 6.5 Å, : τ_r = 334 ps, T_{1E} = 0.41 ps, μ_{eff} = 10.6 B.M.) .

d) Axial images from a 3DGE acquisition in a concentric tube phantom containing 3mM $[Dy.L^1]^-$ solution in the central tube and water only in the outer tube. Upper row of the panel shows the water (left) and $[Dy.L^1]^-$ (right) images using frequency selective excitation of each resonance. Lower row of panel shows dual imaging acquisition using double bandwidth readout and Gaussian signal excitation optimized at the $[Dy.L^1]^-$ frequency. Residual flip angle at the water frequency (20KHz offset) yields the water image.

Figure 2: Biodynamics of $[Gd.L^1]^-$ *in vivo*.

(a) MRI signal intensity curves obtained from selected ROIs using a DCE-MRI sequence.

(b) Measurements of tissue Gd concentration based on invasive tissue sampling. The kidney data (yellow) is shown again overlaid onto the DCE-MRI signal curve (a, left) to illustrate the similarity in time course (despite being in different animals).

Figure 3: PARASHIFT measurements *in vivo.*

(a) PARASHIFT signal from $[Dy.L^1]^-$ (color scale) overlaid onto conventional structural MRI scans. Each column represents a different time point post-injection. Within each column the data represent different spatial axial slices through the mouse. Mean peak ROI signal to noise ratio in this animal was 9.9 in liver, 11.7 in kidney and 18.6 in bladder.

(b) Time series analysis of PARASHIFT concentration from selected ROIs in 6 mice.

Figure 4: PARASHIFT temperature mapping studies.

(a) *In vitro* study of PARASHIFT sample at varying temperatures. Each row presents data collected using a 2D spectroscopic imaging acquisition at the specified sample temperature. The spectral data were reconstructed as images of PARASHIFT peak intensity at each spectral frequency and dependence of shift on temperature is plotted (*right panel*).

(b) *In vivo* PARASHIFT dual imaging experiment showing contrast agent distribution as a function of time and tissue temperature assessment based on the frequency dependence of the PARASHIFT signal. Data were collected using a 3DSI sequence providing a 4D dataset (3D spatial and 1D spectral). The image panel presents the spectral grids for 3 of the MRSI slices acquired 1 minute after i.v. injection (*upper row*) with the same data displayed as the reconstructed PARASHIFT tissue distribution (derived from the peak area for each voxel in the 3DSI experiment) overlaid on the anatomical scans (*middle row*). The tissue concentration data at 25 minutes post injection is show in the *lower row*. The anatomical scans were collected prior to contrast injection and show the location of the PARASHIFT filled tube used for system calibration and as a concentration reference. This sample tube was remotely withdrawn from the FOV before injection and so does not appear in the PARASHIFT images.

PARASHIFT frequency is temperature dependent and can be used to map temperature differences. Spectra (*right panel*) were extracted from selected regions of interest in kidney

at the 1 minute time point and from the bladder at the 25 minutes time point and corrected for differences in B_o field strength in each region based on the water signal frequency. Significant changes in signal frequency (temperature) are apparent over time between kidney and bladder.

Supporting Figure S1: PARASHIFT chemical shift as a function of sample temperature. The chemical shift of the *tert*-butyl group in $[DyL^1]^-$ was measured as a function of temperature in vitro, by high-resolution NMR at 11.7 T (^1H, 500 MHz) both in D_2O (*blue)* and murine plasma (*red*). Linear fitting revealed a dependence of 0.31 ppm K^{-1} in D_2O, and 0.28 ppm K^{-1} in murine plasma, in agreement with the phantom imaging study at 7 T in 0.9 *w/v* % NaCl saline solution of 0.28 ppm K^{-1}.

Supporting Figure S2: Chemical shift of the tert-butyl resonance vs $1 / T^2$ for $[Dy.L^1]^-$ (11.7 T, ^1H) by high-resolution NMR, over the temperature range 290 – 316 K.

Supporting Figure S3: Longitudinal relaxation rate vs $1 / T^2$ for $[DyL^1]^-$: the *tert*-butyl resonance around -60 ppm (11.7 T) was monitored by high-resolution ^1H NMR, over the temperature range 290 – 316 K.

References

1. Caravan P, Ellison JJ, McMurry TJ, Lauffer RB. Gadolinium(III) chelates as MRI contrast agents: Structure, dynamics, and applications. Chemical Reviews 1999;99(9):2293-2352.
2. Chen HH, Wei L, Rotile NJ, Farrar CT, Tanabe KK, Fuchs BC, Caravan P. Quantitative molecular magnetic resonance imaging (MRI) of lysyl oxidase-mediated collagen crosslinking during liver fibrosis. Hepatology 2014;60:205A-205A.
3. Fuchs BC, Wang H, Yang Y, Wei L, Polasek M, Schuehle DT, Lauwers GY, Parkar A, Sinskey AJ, Tanabe KK, Caravan P. Molecular MRI of collagen to diagnose and stage liver fibrosis. Journal of Hepatology 2013;59(5):992-998.
4. Caravan P, Yang Y, Zachariah R, Schmitt A, Mino-Kenudson M, Chen HH, Sosnovik DE, Dai G, Fuchs BC, Lanuti M. Molecular Magnetic Resonance Imaging of Pulmonary Fibrosis in Mice. American Journal of Respiratory Cell and Molecular Biology 2013;49(6):1120-1126.
5. Sibson NR, Blamire AM, Bernades-Silva M, Laurent S, Boutry S, Muller RN, Styles P, Anthony DC. MRI detection of early endothelial activation in brain inflammation. Magnetic Resonance in Medicine 2004;51(2):248-252.
6. Serres S, Soto MS, Hamilton A, McAteer MA, Carbonell WS, Robson MD, Ansorge O, Khrapitchev A, Bristow C, Balathasan L, Weissensteiner T, Anthony DC, Choudhury RP, Muschel RJ, Sibson NR. Molecular MRI enables early and sensitive detection of brain metastases. Proceedings of the National Academy of Sciences of the United States of America 2012;109(17):6674-6679.
7. Ruemenapp C, Gleich B, Mannherz HG, Haase A. Detection of molecules and cells using nuclear magnetic resonance with magnetic nanoparticles. Journal of Magnetism and Magnetic Materials 2015;380:271-275.
8. Coman D, Trubel HK, Rycyna RE, Hyder F. Brain temperature and pH measured by (1)H chemical shift imaging of a thulium agent. Nmr in Biomedicine 2009;22(2):229-239.
9. Hekmatyar SK, Hopewell P, Pakin SK, Babsky A, Bansal N. Noninvasive MR thermometry using paramagnetic lanthanide complexes of 1,4,7,10-tetraazacyclodoecane- alpha,alpha ',alpha ",alpha "'-tetramethyl-1,4,7,10-tetraacetic acid (DOTMA(4-)). Magnetic Resonance in Medicine 2005;53(2):294-303.

10. Zuo CS, Bowers JL, Metz KR, Nosaka T, Sherry AD, Clouse ME. TmDOTP5-: A substance for NMR temperature measurements in vivo. Magnetic Resonance in Medicine 1996;36(6):955-959.
11. Zuo CS, Metz KR, Sun Y, Sherry AD. NMR temperature measurements using a paramagnetic lanthanide complex. J Magn Reson 1998;133(1):53-60.
12. Trubel HKF, Maciejewski PK, Farber JH, Hyder F. Brain temperature measured by H-1-NMR in conjunction with a lanthanide complex. Journal of Applied Physiology 2003;94(4):1641-1649.
13. Sun Y, Sugawara M, Mulkern RV, Hynynen K, Mochizuki S, Albert M, Zuo CS. Simultaneous measurements of temperature and pH in vivo using NMR in conjunction with TmDOTP5. Nmr in Biomedicine 2000;13(8):460-466.
14. Coman D, de Graaf RA, Rothman DL, Hyder F. In vivo three-dimensional molecular imaging with Biosensor Imaging of Redundant Deviation in Shifts (BIRDS) at high spatiotemporal resolution. NMR in biomedicine 2013;26(11):1589-1595.
15. Coman D, Sanganahalli BG, Jiang L, Hyder F, Behar KL. Distribution of temperature changes and neurovascular coupling in rat brain following 3,4-methylenedioxymethamphetamine (MDMA, "ecstasy") exposure. NMR in biomedicine 2015;28(10):1257-1266.
16. Coman D, Trubel HK, Hyder F. Brain temperature by Biosensor Imaging of Redundant Deviation in Shifts (BIRDS): comparison between TmDOTP5- and TmDOTMA(-). Nmr in Biomedicine 2010;23(3):277-285.
17. James JR, Gao Y, Miller MA, Babsky A, Bansal N. Absolute Temperature MR Imaging With Thulium 1,4,7,10-Tetraazacyclododecane-1,4,7,10-Tetramethyl-1,4,7,10-Tetraacetic Acid (TmDOTMA(-)). Magnetic Resonance in Medicine 2009;62(2):550-556.
18. Pakin SK, Hekmatyar SK, Hopewell P, Babsky A, Bansal N. Non-invasive temperature imaging with thulium 1,4,7,10-tetraazacyclododecane-1,4,7,10-tetramethyl-1,4,7,10-tetraacetic acid (TmDOTMA(-)). Nmr in Biomedicine 2006;19(1):116-124.
19. Schmidt R, Nippe N, Strobel K, Masthoff M, Reifschneider O, Castelli DD, Holtke C, Aime S, Karst U, Sunderkotter C, Bremer C, Faber C. Highly Shifted Proton MR Imaging: Cell Tracking by Using Direct Detection of Paramagnetic Compounds. Radiology 2014;272(3):785-795.
20. Chalmers KH, De Luca E, Hogg NHM, Kenwright AM, Kuprov I, Parker D, Botta M, Wilson JI, Blamire AM. Design Principles and Theory of Paramagnetic Fluorine-

Labelled Lanthanide Complexes as Probes for F-19 Magnetic Resonance: A Proof-of-Concept Study. Chemistry-a European Journal 2010;16(1):134-148.

21. Chalmers KH, Kenwright AM, Parker D, Blamire AM. (19)F-Lanthanide Complexes With Increased Sensitivity for (19)F-MRI: Optimization of the MR Acquisition. Magnetic Resonance in Medicine 2011;66(4):931-936.
22. Zhang SR, Merritt M, Woessner DE, Lenkinski RE, Sherry AD. PARACEST agents: Modulating MRI contrast via water proton exchange. Accounts of Chemical Research 2003;36(10):783-790.
23. Harvey P, Blamire AM, Wilson JI, Finney K-LNA, Funk AM, Senanayake PK, Parker D. Moving the goal posts: enhancing the sensitivity of PARASHIFT proton magnetic resonance imaging and spectroscopy. Chemical Science 2013;4(11):4251-4258.
24. Funk AM, Harvey P, Finney KL, Fox MA, Kenwright AM, Rogers NJ, Senanayake PK, Parker D. Challenging lanthanide relaxation theory: erbium and thulium complexes that show NMR relaxation rates faster than dysprosium and terbium analogues. Phys Chem Chem Phys 2015;17(25):16507 - 16511.
25. Hekmatyar SK, Kerkhoff RM, Pakin SK, Hopewell P, Bansal N. Noninvasive thermometry using hyperfine-shifted MR signals from paramagnetic lanthanide complexes. International Journal of Hyperthermia 2005;21(6):561-574.
26. Funk AM, Finney K-LNA, Harvey P, Kenwright AM, Neil ER, Rogers NJ, Senanayake PK, Parker D. Critical analysis of the limitations of Bleaney's theory of magnetic anisotropy in paramagnetic lanthanide coordination complexes. Chemical Science 2015;6(3):1655-1662.
27. Hayes CE, Axel L. Noise performance of surface coils for magnetic resonance imaging at 1.5T. Medical Physics 1985;12(5):604-607.
28. De Luca E, Harvey P, Chalmers KH, Mishra A, Senanayake PK, Wilson JI, Botta M, Fekete M, Blamire AM, Parker D. Characterisation and evaluation of paramagnetic fluorine labelled glycol chitosan conjugates for F-19 and H-1 magnetic resonance imaging. Journal of Biological Inorganic Chemistry 2014;19(2):215-227.
29. Walker-Samuel S, Ramasawmy R, Torrealdea F, Rega M, Rajkumar V, Johnson SP, Richardson S, Goncalves M, Parkes HG, Arstad E, Thomas DL, Pedley RB, Lythgoe MF, Golay X. In vivo imaging of glucose uptake and metabolism in tumors. Nature Medicine 2013;19(8):1067-1072.

30. Li YG, Sheth VR, Liu GS, Pagel MD. A self-calibrating PARACEST MRI contrast agent that detects esterase enzyme activity. Contrast Media & Molecular Imaging 2011;6(4):219-228.
31. Ekanger LA, Allen MJ. Overcoming the concentration-dependence of responsive probes for magnetic resonance imaging. Metallomics 2015;7(3):405-421.
32. Raghunand N, Howison C, Sherry AD, Zhang SR, Gillies RJ. Renal and systemic pH imaging by contrast-enhanced MRI. Magnetic Resonance in Medicine 2003;49(2):249-257.
33. Garcia-Martin ML, Martinez GV, Raghunand N, Sherry AD, Zhang SR, Gillies RJ. High resolution pH(e) imaging of rat glioma using pH-dependent relaxivity. Magnetic Resonance in Medicine 2006;55(2):309-315.
34. McVicar N, Li AX, Suchy M, Hudson RHE, Menon RS, Bartha R. Simultaneous In Vivo pH and Temperature Mapping Using a PARACEST-MRI Contrast Agent. Magnetic Resonance in Medicine 2013;70(4):1016-1025.
35. Yoo B, Sheth VR, Howison CM, Douglas MJK, Pineda CT, Maine EA, Baker AF, Pagel MD. Detection of In Vivo Enzyme Activity with CatalyCEST MRI. Magnetic Resonance in Medicine 2014;71(3):1221-1230.
36. Sheth VR, Li YG, Chen LQ, Howison CM, Flask CA, Pagel MD. Measuring in vivo tumor pHe with CEST-FISP MRI. Magnetic Resonance in Medicine 2012;67(3):760-768.
37. Liu GS, Li YG, Sheth VR, Pagel MD. Imaging In Vivo Extracellular pH with a Single Paramagnetic Chemical Exchange Saturation Transfer Magnetic Resonance Imaging Contrast Agent. Molecular Imaging 2012;11(1):47-57.
38. Longo DL, Sun PZ, Consolino L, Michelotti FC, Uggeri F, Aime S. A General MRI-CEST Ratiometric Approach for pH Imaging: Demonstration of in Vivo pH Mapping with lobitridol. Journal of the American Chemical Society 2014;136(41):14333-14336.

Supporting Material

A new paramagnetically shifted imaging probe for MRI

P. Kanthi Senanayake[3], Nicola J. Rogers[3], Katie-Louise N. A. Finney[3], Peter Harvey[3], Alexander M. Funk[3], J. Ian Wilson[2], Dara O'Hogain[1], Ross Maxwell[2], David Parker[3], Andrew M. Blamire*[1]

Affiliations:

1: Institute of Cellular Medicine & Newcastle MR Centre, Newcastle University

2: Northern Institute for Cancer Research, Newcastle University

3: Dept. of Chemistry, Durham University, South Road, Durham.

Supplementary Figures

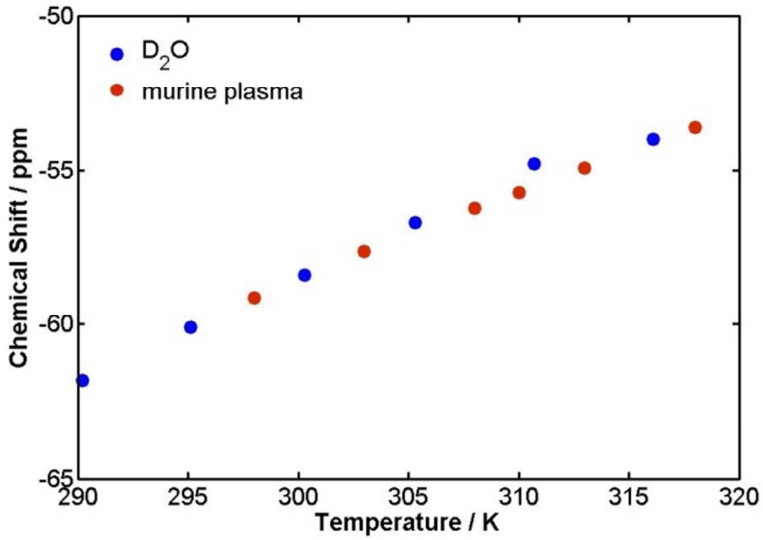

Supporting Figure S1: PARASHIFT chemical shift as a function of sample temperature.

The chemical shift of the *tert*-butyl group in $[Dy.L^1]^-$ was measured as a function of temperature in vitro, by high-resolution NMR at 11.7 T (^1H, 500 MHz) both in D_2O (*blue)* and murine plasma (*red*). Linear fitting revealed a dependence of 0.31 ppm K^{-1} in D_2O, and 0.28 ppm K^{-1} in murine plasma, in agreement with the phantom imaging study at 7 T in 0.9 *w/v* % NaCl saline solution of 0.28 ppm K^{-1}.

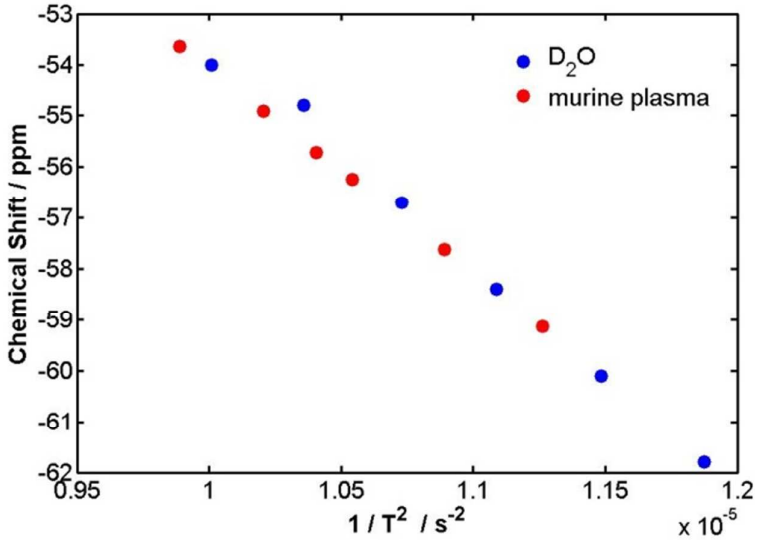

Supporting Figure S2: Chemical shift of the *tert*-butyl resonance vs $1 / T^2$ for $[Dy.L^1]^-$ (11.7 T , ^1H) by high-resolution NMR, over the temperature range 290 – 316 K.

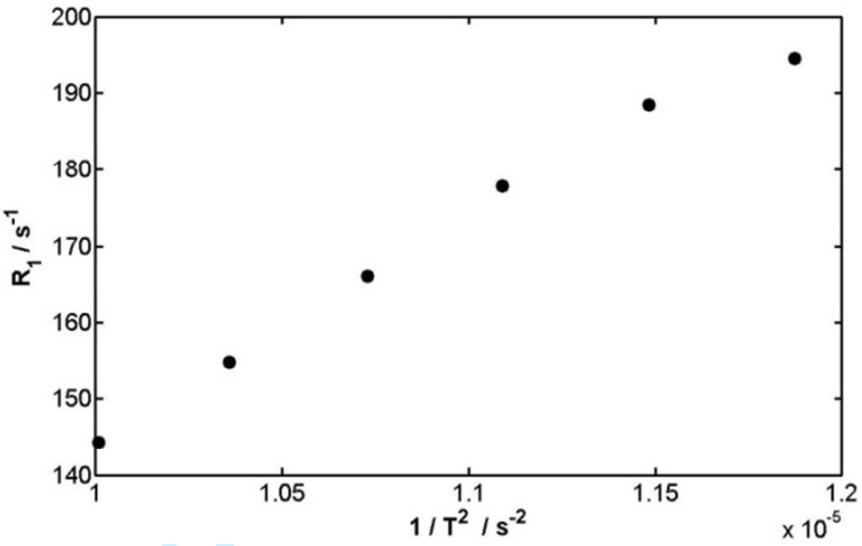

Supporting Figure S3: Longitudinal relaxation rate vs 1 / T^2 for [Dy.L^1]$^-$: the *tert*-butyl resonance around -60 ppm (11.7 T) was monitored by high-resolution ^{1}H NMR, over the temperature range 290 – 316 K.

Supplementary Methods

Measurement of NMR relaxation characteristics of [Dy.L^1]$^-$

High-resolution NMR field-dependent R_1 measurements were made, examining the *tert*-butyl resonance of [Dy.L^1]$^-$. Proton NMR spectra were obtained at 295 K on Varian spectrometers operating at 4.7, 9.4, 11.7, 14.1 and 16.5 Tesla, specifically on a Mercury 200 spectrometer (^{1}H at 200.057 MHz), a Mercury 400 spectrometer (^{1}H at 399.97 MHz), a Varian Inova-500 spectrometer (^{1}H at 499.78 MHz), a Varian VNMRS-600 spectrometer (^{1}H at 599.944 MHz) and a Varian VNMRS-700 spectrometer (^{1}H at 700.000 MHz). Commercially available deuterated solvents were used. Measurements at 1T (42.5MHz ^{1}H) were made on a Magritek Spinsolve spectrometer. The operating temperature was measured using an internal calibration sample of neat ethylene glycol.

The nuclear relaxation times of the *tert*-butyl group were measured at the 6 field strengths using the inversion-recovery technique. The incremented delay time was set to span full inversion through full recovery to equilibrium of the signal. The recorded free induction decays were processed using backward linear prediction, optimal exponential weighting, zero-filling, Fourier transformation, phasing and baseline correction (by Whittaker smoothing), if necessary.

Methods for analysis of tissue content of [Gd.L^1]$^-$

Tissue samples (n=3 per tissue, per animal) were taken from the kidney and liver and stored at -80 ^{o}C prior to analysis. Plasma samples were also taken at each time point and frozen. Weighed tissue samples (typically 10 mgs each) or a fixed aliquot of plasma (0.2 mL) were transferred into separate sample vials. Concentrated nitric acid (0.8 mL) was added and each mixture held at room temperature for a week, generating a clear pale yellow solution. The solutions were diluted to a volume of 2 mL using distilled water. Each sample was analyzed in triplicate by inductively coupled plasma mass spectrometry (ICP-MS) using a Thermo Finnigan ELEMENT light resolution select field ICP-Mass spectrometer; the mean Gd value is given; a blank sample was also run.

Ligand and Complex synthesis

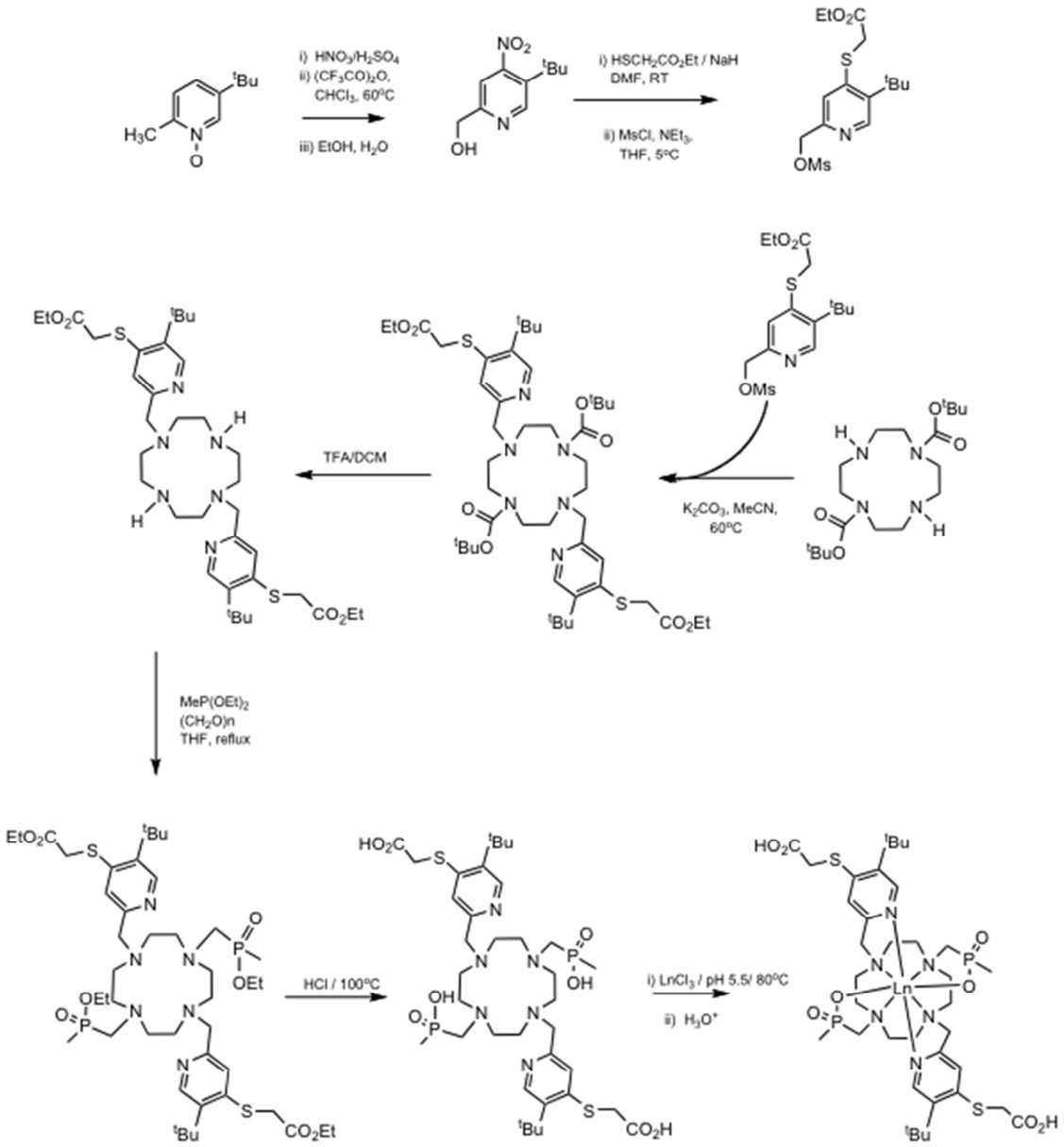

HPLC

Reverse phase HPLC was performed at 295 K using a Shimadzu system comprising a Degassing Unit (DGU-20A_{5R}), a Prominence Preparative Liquid Chromatography pump (LC-20AP), a Prominence UV-Vis Detector (SPD-20A) and Communications Bus Module (CBM-20A). For preparative HPLC an XBridge C18 OBD column was used (19 x 100 mm, 5 µm) with a flow rate of 17 mL/min. For analytical HPLC a Shimadzu Shim-Pack VP-ODS column was used (4.6 x 150 mm, 5 µm) with a flow rate of 2.0 mL/min. Fraction collection was performed manually. A solvent system of H_2O (0.1% HCOOH) / CH_3OH (0.1% HCOOH) was used with gradient elution as follows:

Time / min	%H_2O	%CH_3OH
0	90	10
3	90	10
13	0	100
16	0	100
17	90	10

5-*tert*-Butyl-2-methyl -4 nitropyridine 1-oxide

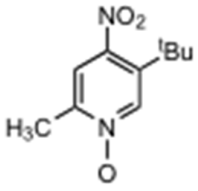

5-*tert*-Butyl-2-methylpyridine 1-oxide (1.2 g, 6 mmol) was taken into H_2SO_4 (2 ml), and HNO_3 (1.5 ml) was added at 0°C. The reaction mixture was heated at 100°C overnight and poured onto ice. The product was extracted using dichloromethane dried over $MgSO_4$ and the solvent was removed under vacuum to give a colourless oil (1.1 g.73%). ^{1}H NMR (400 MHz,$CDCl_3$): δ 8.42 (s, 1H, H^6), 7.33 (s,1H, H^3), 2.50 (s, 3H, Me), 1.47 (s, 9H, ^{t}Bu). ^{13}C NMR (101 MHz, $CDCl_3$): δ = 147.4 (C^2), 145.7 (C^6), 137.4 (C^5), 131.7 (C^3), 116.7 (C^4), 33.6 ($\underline{C}(CH)_3$), 30.6 ($C(\underline{C}H)_3$), 16.9($\underline{C}H_3$);); ESI-LRMS (+) *m/z* 210.1 $[M+H]^+$; ESI-HRMS (+) calcd for $C_{10}H_{15}N_2O_3$ 211.1069, found 211.1079.

(5-*tert*-Butyl-4-nitropyridin-2-yl)methanol

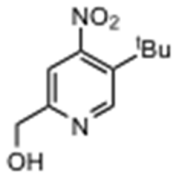

Trifluoroacetic anhydride (30 mL) was added to a solution of 5-*tert*-butyl-4-nitro-2-methylpyridine 1-oxide (1.6g, 7.5 mmol) in DCM (30 mL). The resulting mixture was heated at 60°C for 18 h under an inert atmosphere. After this time, the solvent was removed under reduced pressure and reaction completion to the trifluoroacetate intermediate was confirmed by ^{1}H NMR analysis. The resulting bright yellow oil was stirred in a mixture of EtOH (5 mL) and H_2O (5mL) for 1 h. The solvent was removed and the residue was taken into ethyl acetate (20ml). The organic layer was washed with dilute aqueous sodium hydroxide solution, dried over $MgSO_4$ and solvent was removed under reduced pressure to yield a yellow oil (1.1g, 69 %); ^{1}H NMR (400 MHz, $CDCl_3$): δ 8.76 (s, 1H, H^6), 7.27 (s, H^3), 4.78 (s, 2H, $C\underline{H}_2OH$), 1.39 (s, 9H, ^{t}Bu); ^{13}C NMR (101 MHz, $CDCl_3$): δ 161.1(C^4), 157.5(C^2), 150.5(C^3), 133.5(C^5), 114.0 (C^6), 64.0($\underline{C}H_2OH$), 34.6($\underline{C}(CH)_3$), 30.5($C(\underline{C}H)_3$); ESI-LRMS (+) *m/z* 211 $[M+H]^+$; ESI-HRMS (+) calcd for $C_{10}H_{15}N_2O_3$ 211.1069, found 211.1073.

(5-*tert*-Butyl-4 ethyl thioglycolate-pyridin-2-yl)methanol

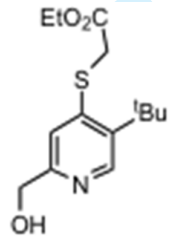

Ethyl thioglycolate (1.7 ml, 14.4 mmol) and sodium hydride (0.8g, 33 mmol) were taken into anhydrous dimethylformamide (3 ml), and (5-*tert*-butyl-4-nitropyridin-2-yl)methanol (1.0g, 4.8mmol) in DMF (2 ml) was added at RT and the solution was stirred for an hour. Dimethyl formamide was removed under reduced pressure and the residue was taken to dichloromethane. Inorganic salts were filtered off and solvent was removed. The crude residue was purified using silica column chromatography, eluting with a gradient starting from DCM to 2 % MeOH/DCM to yield a yellow oil (0.45 g, 30 %), R_f (5 % MeOH / DCM) = 0.4); ^{1}H NMR (400 MHz, $CDCl_3$): δ 8.43 (s, 1H, H^6), 7.22 (s, H^3), 4.68 (s, 2H, $C\underline{H}_2OH$),4.19 (q, J = 7 Hz, 2H, $OC\underline{H}_2$), 3.78 (s, 2H, $SC\underline{H}_2$), 1.49 (s, 9H, ^{t}Bu), 1.24 (t, 3H, J = 7 Hz, $CH_2\underline{C}H_3$) ; ^{13}C NMR (101 MHz, $CDCl_3$): δ 168.1(C=O), 157.5(C^4), 147.9(C^2),

145.8(C^5), 140.0 (C^3), 118.4(C^6),, 64.2($\underline{C}H_2OH$), 62.2 ($O\underline{C}H_2$) 35.4 ($S\underline{C}H_2$), (34.6($\underline{C}(CH)_3$), 30.5($C(\underline{C}H)_3$); ESI-LRMS (+) *m/z* 284 $[M+H]^+$; ESI-HRMS (+) calcd for $C_{14}H_{22}NO_3S$ 284.1320, found 284.1314.

(5-*tert*-Butyl-4 ethyl thioglycolate-pyridin-2-yl)methyl-methanesulphonate

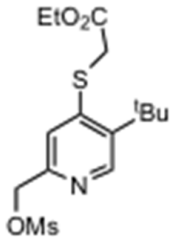

5-*tert*-Butyl-4 ethyl thioglycolate-pyridin-2-yl)methanol (450 mg, 1.60 mmol) was dissolved in THF (10 mL) and cooled to 5°C. Triethylamine (0.35 mL, 3.20 mmol) and mesyl chloride (0.20 mL, 2.40 mmol) were added dropwise to this solution. Once addition was complete, the reaction mixture was allowed to warm to RT and stirred for 2 h, before the solvent was removed under reduced pressure. The residue was treated with brine (10 mL) and extracted with DCM (2 x 10 mL). The organic layers were combined, dried over $MgSO_4$, and the solvent removed under reduced pressure to yield an orange oil, which was used immediately (500 mg, 87 %). R_f (10 % MeOH/DCM) = 0.56; ^{1}H NMR (400 MHz, $CDCl_3$): δ 8.68 (d, J = 2 Hz, 1H, H^6),7.52 (d, J = 8 Hz, 1H, H^3), 5.39 (s, 2H, $C\underline{H}_2OMs$), 3.78 (s, 2H, $SC\underline{H}_2$), 3.12 (s, 3H, $SO_2C\underline{H}_3$), 1.37 (s, 9H, ^{t}Bu); ESI-LRMS (+) *m/z* 244.2 $[M+H]^+$; ESI-HRMS (+) calcd for $C_{11}H_{17}NO_3S$ 244.1007, found 244.1020

Di-tert-butyl 4,10-bis((5-(tert-butyl)-4-((2-ethoxy-2-oxoethyl)thio)pyridin-2-yl)methyl)-1,4,7,10-tetraazacyclododecane-1,7-dicarboxylate

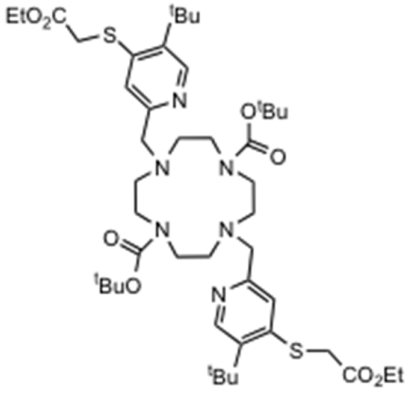

Di-tert-butyl 1,4,7,10-tetraazacyclododecane-1,7-dicarboxylate (0.3g,0.75mmol) was dissolved in acetonitrile (30ml) and (5-*tert*-butyl-4 ethyl thioglycolate-pyridin-2-yl)methyl-methanesulphonate (0.65g, . 1.87mmol) and potassium carbonate (0.22g, 1.65mmol) were added. The reaction mixture was heated at 80°C for 10h. Inorganic salts were filtered off and solvent was removed under reduced pressure to give a pale yellow oily product. The crude residue was purified using silica column chromatography, eluting with a gradient starting from DCM to 5 % MeOH/DCM to yield an oily product (330mg, 50%). R_f (5 % MeOH/DCM) = 0.2). ^{1}H NMR (400 MHz, $CDCl_3$): δ = 8.41 (s, 2H, H^6), 7.26 (s, 2H, H^3), 4.19(2xt, J = 4 Hz, 4H, OCH_2CH_3), 3.96 (s,4H, $SCH2$), 3.83 (s, 2H, NCH_2Py),3.74(s, 2H, NCH_2Py) , (3.49-3.37 (br m, 12H, cyclen-CH_2),2.78-2.62 (br m, 4H, cyclen-CH_2), 1.51 (s, 18H, ^{t}Bu), 1.27 (s, 18H, ^{t}Bu), 1.24 (t, J= 4Hz, 6H, CH_2CH_3); ^{13}C NMR (101 MHz, CDCl3): δ = 168.8 (CO_2Et), 155.9 (CO_2tBu), 146.6 (C^4), 143.8(C^2), 140.7 (C^5), 120.8 (C^3), 119.7 (C^6), 61.9 (OCH_2), 60.2 (NCH_2Py), 58.2 (cyclen–CH_2), 54.6 (cyclen-CH_2), 52.8 (cyclen-CH_2), 52.4 (cyclen-CH_2), 46.3 (cyclen-CH_2), 48.3 (cyclen-CH_2), 35.4 (SCH_2) 35.4 ($C(CH_3)_3$), 29.8 ($C(CH)_3$), 28.5 ($C(CH_3)_3$), 14.3(CH_2CH_3); ESI/MS+ m/z 903.5 [M+H]+, HRMS Calcd for $C_{46}H_{75}N_6O_8S_2$ 903.5088. Found 903.5117

Diethyl 2,2'-((((1,4,7,10-tetraazacyclododecane-1,7-diyl)bis(methylene))bis(5-(tert-butyl)pyridine-2,4-diyl))bis(sulfanediyl))diacetate

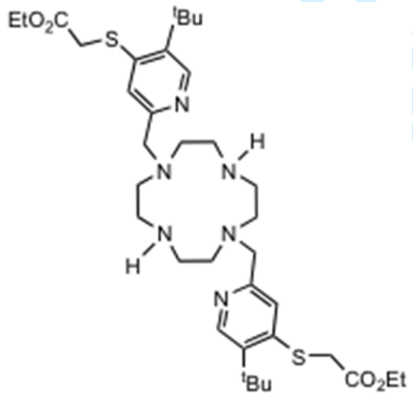

Di-tert-butyl 4,10-bis((5-(tert-butyl)-4-((2-ethoxy-2-oxoethyl)thio)pyridin-2-yl)methyl)-1,4,7,10-tetraazacyclododecane-1,7-dicarboxylate (0.33g, 0.37mmol) was taken to dichloromethane (2ml) and trifluoroacetic acid (2ml) was added and stirred at room temperature for 18h. The solvent was removed and dichloromethane (2ml) was added and removed under reduced pressure (repeated three times) to remove traces of trifluoroacetic

acid. The residue was taken into water (2ml) and pH was adjusted using dilute sodium hydroxide solution to 10-11. The product was extracted using dichloromethane, dried using $MgSO_4$ and solvent was removed under reduced pressure to give a clear oily product (0.25g, 96%). ^{1}H NMR (400 MHz, $CDCl_3$): δ = 8.44 (s, 2H, H^6), 7.63 (s, 2H, H^3), 4.18 (q, J = 4 Hz, 4H, $OC\underline{H}_2CH_3$), 3.96 (s,4H, $SC\underline{H}_2$), 3.99 (s, 4H, $NC\underline{H}_2Py$), 3.23 (br m, 8H, cyclen-$C\underline{H}_2$),3.14 (br m, 8H, cyclen-$C\underline{H}_2$), 1.48 (s, 18H, ^{t}Bu), 1.24 (t, J = 7 Hz, 6H, $CH_2C\underline{H}_3$); ^{13}C NMR (101 MHz, $CDCl_3$): δ = 168.8 ($\underline{C}O_2Et$), 156.6 (C^4), 149.8(C^2), 143.7 (C^5), 142.1 (C^3), 122.53 (C^6), 61.9 ($O\underline{C}H_2$), 60.2 ($S\underline{C}H_2$), 55.1 ($N\underline{C}H_2Py$), 53.5(cyclen–$\underline{C}H_2$), 49.1 (cyclen-$\underline{C}H_2$), 43.5 (cyclen-$\underline{C}H_2$), 35.4 ($S\underline{C}H_2$) 35.4 ($\underline{C}(CH_3)_3$), 29.8 ($C(\underline{C}H)_3$), 28.9 ($C(\underline{C}H_3)_3$), 14.1($CH_2\underline{C}H_3$); ESI/MS+ m/z 702.5 [M+H]+, HRMS Calcd for $C_{36}H_{59}N_6O_4S_2$ 703.4039. Found 703.4063

Diethyl 2,2'-((((4,10-bis((ethoxy(methyl)phosphoryl)methyl)-1,4,7,10-tetraazacyclododecane-1,7-diyl)bis(methylene))bis(5-(tert-butyl)pyridine-2,4-diyl))bis(sulfanediyl))diacetate

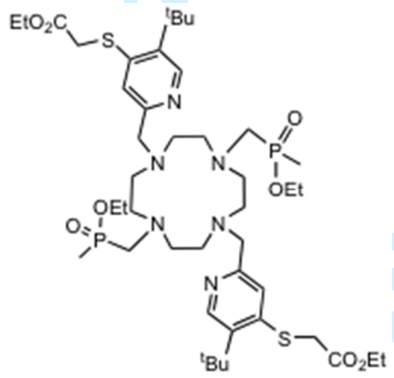

Diethyl 2,2'-((((1,4,7,10-tetraazacyclododecane-1,7-diyl)bis(methylene))bis(5-(tert-butyl)pyridine-2,4-diyl))bis(sulfanediyl))diacetate (0.3g, 0.43mmol)was dissolved anhydrous THF (25ml). Paraformaldehyde (0.21g, excess) was added and the solution was boiled under reflux over molecular sieves (4Å) using a Soxhlet condenser under argon. Methyl diethoxy phosphine (0.3g, 1.6mmol) was added and continued to heat at reflux temperature for 18hrs. Inorganic salts were filtered off, and solvent was removed under reduced pressure to give an orange oily product. The crude residue was purified using alumina column chromatography eluting with a gradient starting from DCM to 2 % MeOH/DCM to yield a yellow oil (160mg, 40%). R_f (10 % MeOH/DCM) = 0.25). ^{1}H NMR (400 MHz, $CDCl_3$): δ = 8.44 (s, 2H, H^6),

7.97 (s, 1H, H^3), 7.45 (s, 1H, H^3), 4.17(q, J = 7 Hz, 4H, OCH_2CH_3), 4.07 (m, 4H, $POCH_2$), 3.84 (s,4H, SCH_2), 3.71 (s, 2H, NCH_2 py),3.64(s, 2H, NCH_2py) , (3.07-2.94 (br m, 4H, PCH_2), 2.78-2.58 (br m, 12H, cyclen-CH_2), 2.49-2.38(br m, 4H,cyclen-CH_2), 1.49 (s, 18H, tBu), 1.43 (d, J = 16 Hz, 6H, PCH_3), 1.26 (t, J = 7 Hz, 6H, CH_2CH_3), 1.21(t, J= 4 Hz, 6H, CH_2CH_3); ^{13}C NMR (101 MHz, $CDCl_3$): δ = 168.8 (CO_2Et), 156.7 (C^4), 146.7, 146.4(C^2), 140.6, 140.5 (C^5), 122.8, 121.2 (C^3), 120.7 (C^6), 61.9 (OCH_2),61.1(POCH2) 60.2 (NCH_2py), 55.4 (cyclen–CH_2), 55.0 (cyclen-CH_2), 54.3 (cyclen-CH_2), 53.5 (cyclen-CH_2), 53.0 (cyclen-CH_2), 52.2 (cyclen-CH_2),47.3 (NCH_2P) 35.4, 35.3 (SCH_2) 35.6 ($C(CH_3)_3$), 29.9 ($C(CH)_3$), 28.5 ($C(CH_3)_3$), 16.9 (CH_2CH_3), 14.3(CH_2CH_3); ^{31}P NMR (162 MHz, $CDCl_3$) δ = 53.2; ESI/MS+ m/z 942.5 [M+H]+, HRMS Calcd for $C_{44}H_{76}N_6O_8P_2S_2$ 943.4720. Found 943.4741

2,2'-((((4,10-Bis((hydroxy(methyl)phosphoryl)methyl)-1,4,7,10-tetraazacyclododecane-1,7-diyl)bis(methylene))bis(5-(tert-butyl)pyridine-2,4-diyl))bis(sulfanediyl))diacetic acid , L^1.

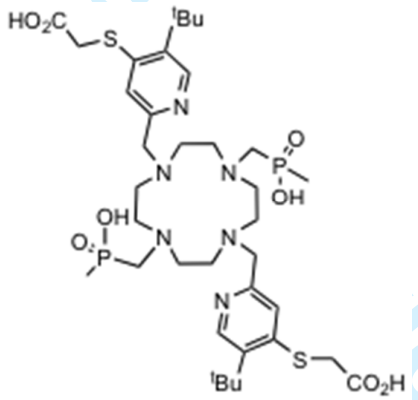

Diethyl 2,2'-((((4,10-bis((ethoxy(methyl)phosphoryl)methyl)-1,4,7,10-tetraazacyclododecane-1,7-diyl)bis(methylene))bis(5-(tert-butyl)pyridine-2,4 diyl))bis(sulfanediyl))diacetate (0.16g, 0.16mmol) was dissolved in hydrochloric acid (6M, 10ml) and heated at80°C for 18 hrs. Water was removed under reduced pressure and the residue was washed with dichloromethane to give a glassy solid (0.12g, 85%).). ^{1}H NMR (400 MHz, CD_3OD): δ = 8.49 (s, 1H, H^6), 8.44 (s, 1H, H^6) 8.06 (br s , 1H, H^3), 7.91 (s, 1H, H^3, 4.47 (s,4H, SCH_2), 4.37 (s, 2H, NCH_2py),4.37(s, 2H, NCH_2py) , (4.04-4.08 (br m, 4H, PCH_2),3.94-3.42 (br m, 12H, cyclen-$CH_2$3.32-2.91(br m, 4H,cyclen-CH_2), 1.62 (s, 18H, tBu), 1.61 (d, J = 16Hz, 6H, PCH_3); ^{13}C NMR (101 MHz, CD_3OD): δ = 174.5 (C=O), 159.7 (C^4), 147.7, 146.4(C^2), 142.6, 140.5 (C^5), 125 (C^3), 122.7 (C^6), , 62.2 (NCH_2Py), 55.4

(cyclen–CH_2), 55.0 (cyclen-CH_2), 54.3 (cyclen-CH_2), 53.5 (cyclen-CH_2), 53.0 (cyclen-CH_2), 52.2 (cyclen-$\underline{C}H_2$), 47.3 ($N\underline{C}H_2P$) 35.4, 35.3 ($S\underline{C}H_2$), 35.6 ($\underline{C}(CH_3)_3$), 28.5 ($C(\underline{C}H_3)_3$; ^{31}P NMR (162 MHz, $CDCl_3$) δ = 30.1; ESI/MS+ m/z 830.3 [M+H]+, HRMS Calcd for $C_{36}H_{61}N_6O_8P_2S_2$ 831.3468. Found 831.3465; m.p : >170°C (dec)

[DyL^1]

Dy(III)$Cl_3.6H_2O$ (27 mg, 0.06mmol) was added to a solution of 2,2'-((((4,10-bis((hydroxy(methyl)phosphoryl)methyl)-1,4,7,10-tetraazacyclododecane-1,7-diyl)bis(methylene))bis(5-(tert-butyl)pyridine-2,4-diyl))bis(sulfanediyl))diacetic acid (L_4) (40mg, 0.05 mmol) dissolved in H_2O (3 mL). The pH was adjusted to 5.5 before stirring the solution for 18 h at 80°C. After this time, the solution was allowed to cool to RT before the pH was raised to 10 using NaOH solution, causing a white solid to precipitate out. This precipitate was removed by centrifugation and the pH of the resulting solution was neutralised using HCl (1M). The solvent was removed under reduced pressure to yield a yellow solid, (30 mg, 98 %). The complex was purified using reverse phase HPLC (t_R = 7.5 min). ^{1} NMR (400 MHz, D_2O, pD 6.9, 295K): δ = -60.15 major, -64.25 minor (^{t}Bu); ESI/MS$^+$ m/z 991.5 $[M]^+$; HRMS Calcd for $C_{36}H_{58}{}^{160}DyN_6O_8P_2S_2$ 988.2508. Found 988.2508

[Gd L^1]

An analogous procedure to that described for **[Dy.L^1]** was followed using Gd(III)$Cl_3.6H_2O$ and solution of 2,2'-((((4,10-bis((hydroxy(methyl)phosphoryl)methyl)-1,4,7,10-tetraazacyclododecane-1,7-diyl)bis(methylene))bis(5-(tert-butyl)pyridine-2,4-diyl))bis(sulfanediyl))diacetic acid (L_4). ESI/MS$^+$ m/z 986.5 $[M]^+$; HRMS Calcd for $C_{36}H_{58}{}^{155}GdN_6O_8P_2S_2$ 983.2459. Found 983.2474. r_{1p} : 2.4 mM^{-1} s^{-1} (pH 6, 1.4 T, 310 K) HPLC : t_R = 7.5 min.

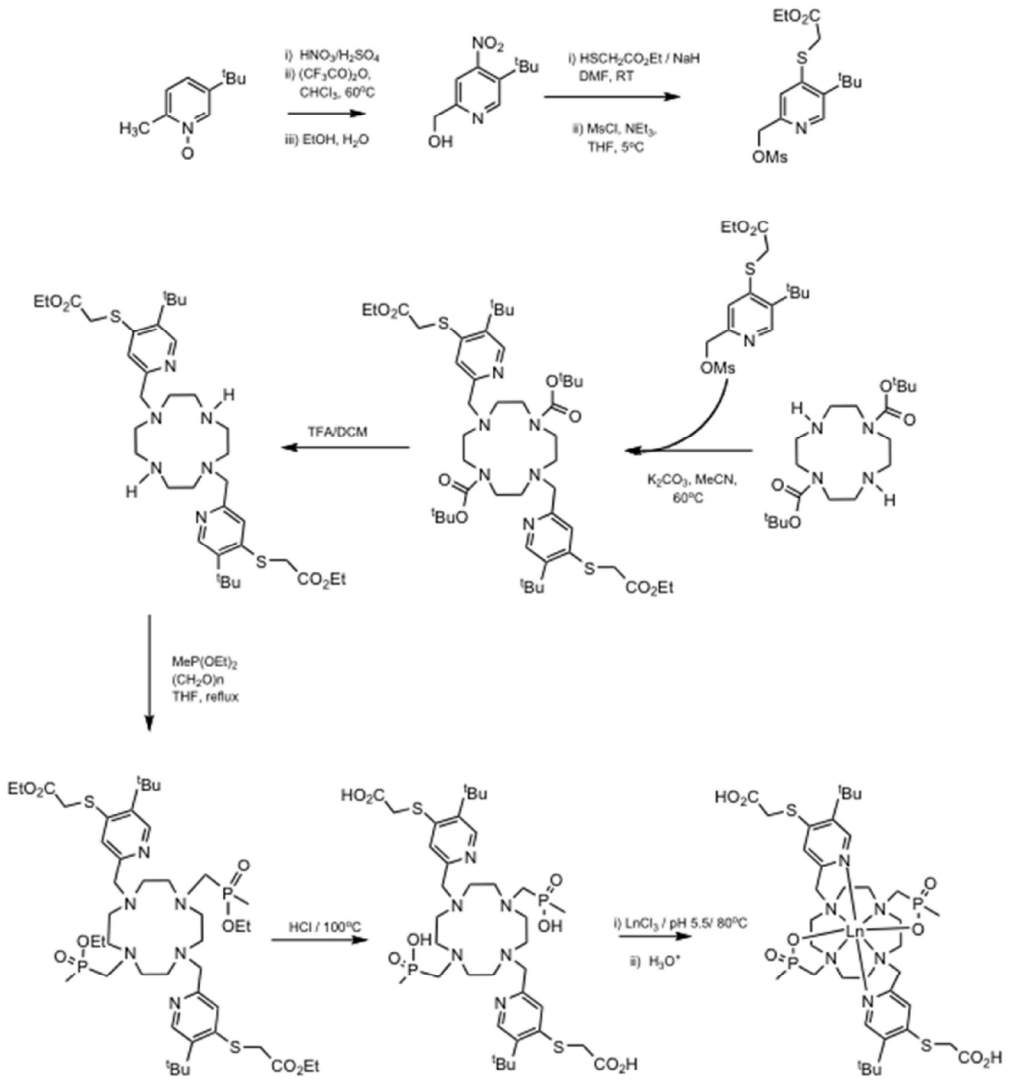

Scheme 1: Synthesis scheme for the $[Ln.L^1]^-$ complexes, where Ln was either Gd or Dy.
139x149mm (300 x 300 DPI)

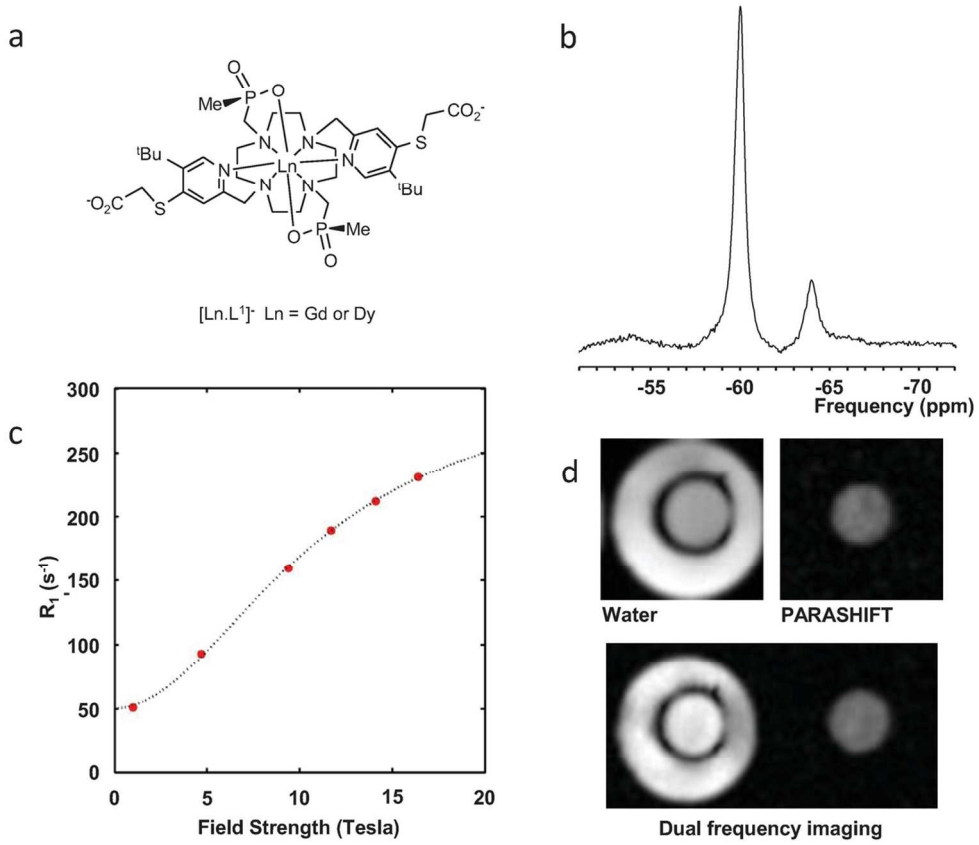

Figure 1: Structure and properties of the PARASHIFT complex
a) Structure of $[Ln.L^1]^-$.
b) Proton spectrum collected on a 7 T preclinical imaging scanner from the tert-butyl signal region (centered at -60.1 ppm) for $[Dy.L^1]^-$. The signal was measured from 100 µL of 6 mM solution using a volume imaging coil, with a 1ms long Gaussian 90o excitation pulse, 20 kHz spectral width, TR = 55 ms, 32 averages and a total acquisition time of 1.76 s. The long RF pulse was used to narrow the bandwidth and prevents excitation of water, but leads to a first order phase difference between the major and minor resonances. The major resonance at -60.1 ppm yields 88% of the signal with the minor resonance at -63.8 ppm the remaining 12% signal.
c) Longitudinal relaxation rates for $[Dy.L^1]^-$ as a function of magnetic field, (D2O 295 K) showing the fit (line) of the Solomon-Morgan-Bloembergen equation to the data (fixed r = 6.5 Å, : μ_r = 334 ps, T1E = 0.41 ps, μ_{eff} = 10.6 B.M.) .

112x96mm (300 x 300 DPI)

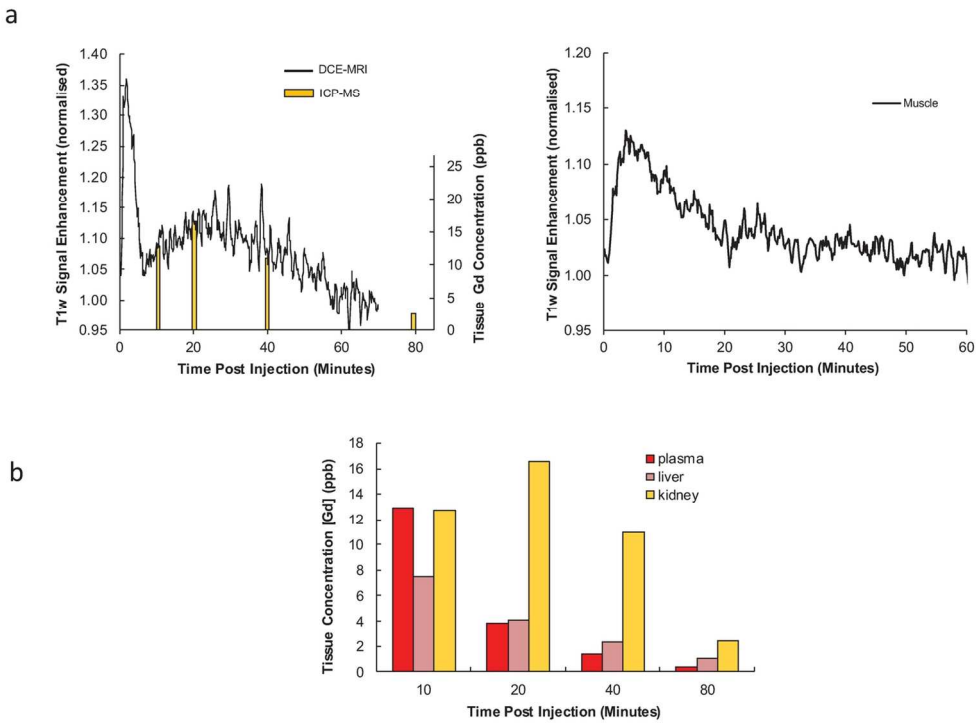

Figure 2: Biodynamics of $[Gd.L^1]^-$ in vivo.
(a) MRI signal intensity curves obtained from selected ROIs using a DCE-MRI sequence.
(b) Measurements of tissue Gd concentration based on invasive tissue sampling. The kidney data (yellow) is shown again overlaid onto the DCE-MRI signal curve (a, left) to illustrate the similarity in time course (despite being in different animals).
131x98mm (300 x 300 DPI)

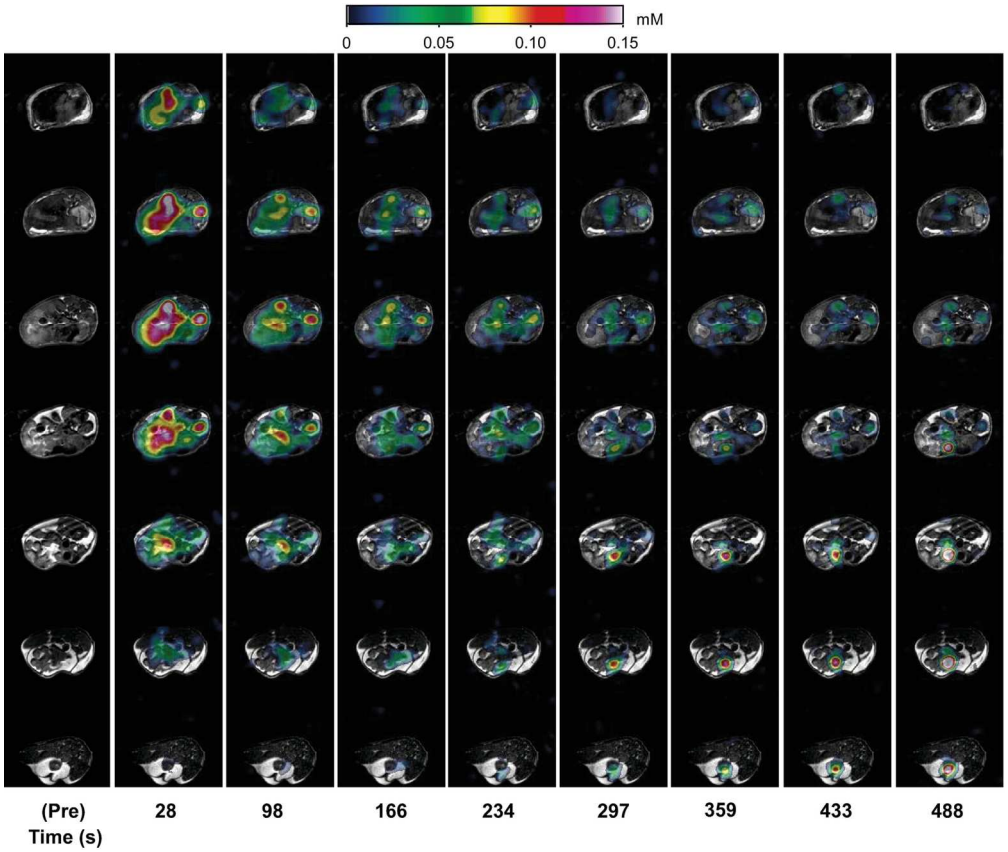

Figure 3: PARASHIFT measurements in vivo.
(a) PARASHIFT signal from $[Dy.L^1]^-$ (color scale) overlaid onto conventional structural MRI scans. Each column represents a different time point post-injection. Within each column the data represent different spatial axial slices through the mouse. Mean peak ROI signal to noise ratio in this animal was 9.9 in liver, 11.7 in kidney and 18.6 in bladder.
150x128mm (300 x 300 DPI)

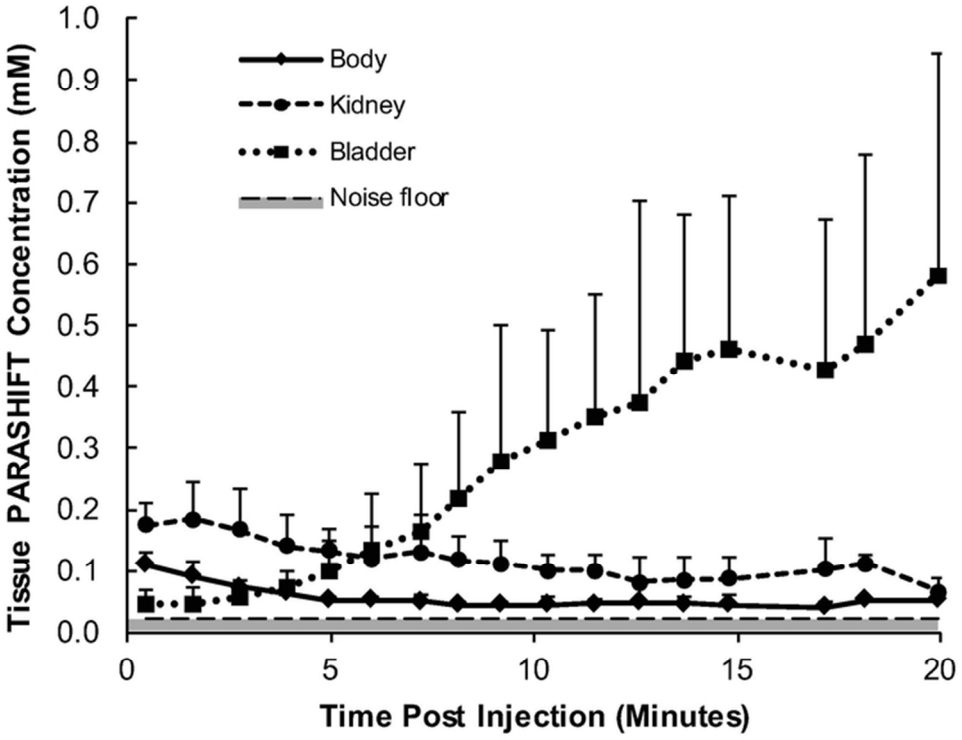

Figure 3: PARASHIFT measurements in vivo.
(b) Time series analysis of PARASHIFT concentration from selected ROIs in 6 mice.
66x50mm (300 x 300 DPI)

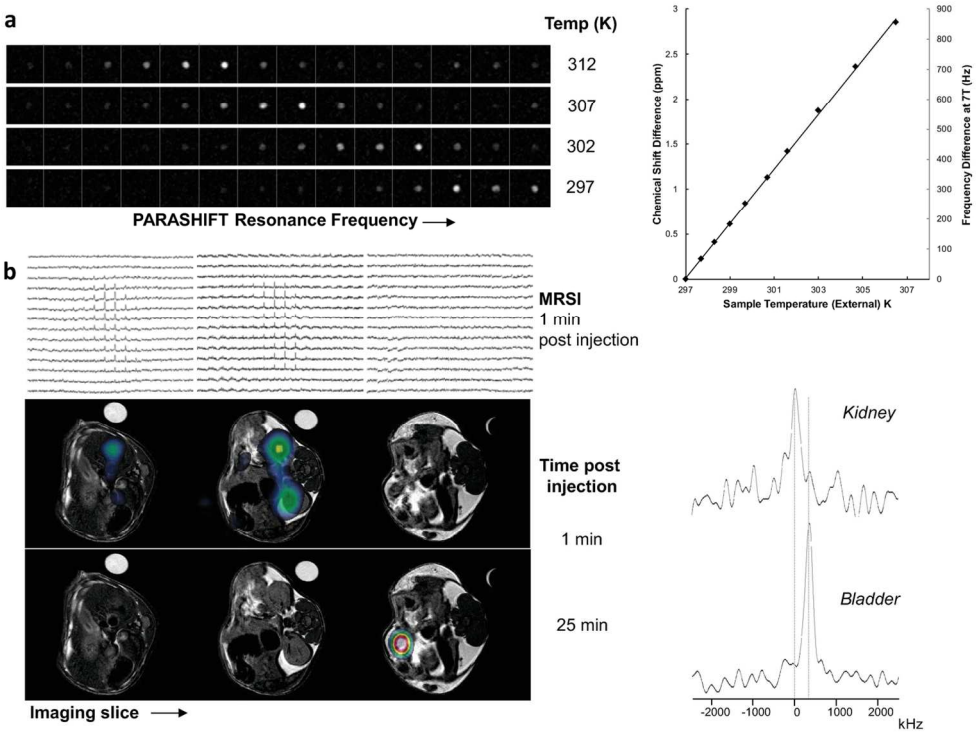

Figure 4: PARASHIFT temperature mapping studies.
(a) In vitro study of PARASHIFT sample at varying temperatures. Each row presents data collected using a 2D spectroscopic imaging acquisition at the specified sample temperature. The spectral data were reconstructed as images of PARASHIFT peak intensity at each spectral frequency and dependence of shift on temperature is plotted (right panel).
(b) In vivo PARASHIFT dual imaging experiment showing contrast agent distribution as a function of time and tissue temperature assessment based on the frequency dependence of the PARASHIFT signal. Data were collected using a 3DSI sequence providing a 4D dataset (3D spatial and 1D spectral). The image panel presents the spectral grids for 3 of the MRSI slices acquired 1 minute after i.v. injection (upper row) with the same data displayed as the reconstructed PARASHIFT tissue distribution (derived from the peak area for each voxel in the 3DSI experiment) overlaid on the anatomical scans (middle row). The tissue concentration data at 25 minutes post injection is show in the lower row. The anatomical scans were collected prior to contrast injection and show the location of the PARASHIFT filled tube used for system calibration and as a concentration reference. This sample tube was remotely withdrawn from the FOV before injection and so does not appear in the PARASHIFT images.
130x97mm (300 x 300 DPI)